Entangled Mesh Hydrogels with Macroporous Topologies via Cryogelation for Rapid Atmospheric Water Harvesting

Jiajun Sun, Feng Ni,* Jincui Gu, Muqing Si, Depeng Liu, Chang Zhang, Xiaoxue Shui, Peng Xiao,* and Tao Chen*

Sorption-based atmospheric water harvesting (SAWH) is a promising technology to alleviate freshwater scarcity. Recently, hygroscopic salt-hydrogel composites (HSHCs) have emerged as attractive candidates with their high water uptake, versatile designability, and scale-up fabrication. However, achieving high-performance SAWH applications for HSHCs has been challenging because of their sluggish kinetics, attributed to their limited mass transport properties. Herein, a universal network engineering of hydrogels using a cryogelation method is presented, significantly improving the SAWH kinetics of HSHCs. As a result of the entangled mesh confinements formed during cryogelation, a stable macroporous topology is attained and maintained within the obtained entangled-mesh hydrogels (EMHs), leading to significantly enhanced mass transport properties compared to conventional dense hydrogels (CDHs). With it, corresponding hygroscopic EMHs (HEMHs) simultaneously exhibit faster moisture sorption and solar-driven water desorption. Consequently, a rapid-cycling HEMHs-based harvester delivers a practical freshwater production of 2.85 L_{water} $kg_{sorbents}^{-1}$ day^{-1} via continuous eight sorption/desorption cycles, outperforming other state-of-the-art hydrogel-based sorbents. Significantly, the generalizability of this strategy is validated by extending it to other hydrogels used in HSHCs. Overall, this work offers a new approach to efficiently address long-standing challenges of sluggish kinetics in current HSHCs, promoting them toward the next-generation SAWH applications.

J. Sun, J. Gu, M. Si, D. Liu, X. Shui, P. Xiao, T. Chen
Key Laboratory of Advanced Marine Materials
Ningbo Institute of Materials Technology and Engineering
Chinese Academy of Sciences
Ningbo 315201, China
E-mail: xiaopeng@nimte.ac.cn; tao.chen@nimte.ac.cn
J. Sun, J. Gu, M. Si, D. Liu, P. Xiao, T. Chen
School of Chemical Sciences
University of Chinese Academy of Sciences
Beijing 100049, China
F. Ni
Max Planck Institute of Microstructure Physics
06120 Halle (Saale), Germany
E-mail: feng.ni@mpi-halle.mpg.de
C. Zhang
School of Biological and Chemical Engineering
NingboTech University
Ningbo 315100, China

The ORCID identification number(s) for the author(s) of this article can be found under https://doi.org/10.1002/adma.202314175

1. Introduction

Water covers 70% of the earth, however, freshwater, a necessity for daily life, is exceedingly scarce. Moreover, freshwater constitutes only 2.5% of the global water, with two-thirds concealed in frozen glaciers or otherwise unavailable to us.[1,2] This challenge intensifies with the continued growth of the worldwide population, the escalating pollution of accessible freshwater resources, and the heightened impacts of climate shifts.[3–6] Over 50% of the global population is anticipated to face freshwater scarcity by 2050, mainly threatening sustainable society development.[7,8] With an estimated amount of ≈12 900 billion tons, atmospheric water represents a potential freshwater resource, yet largely unexplored.[9,10] Therefore, extracting it for freshwater production is a promising solution to mitigate global freshwater scarcity.[11–13] Recently, sorption-based atmospheric water harvesting (SAWH) technology has demonstrated diverse distinct advantages, including broad humidity applicability, decentralized feasibility, and energy-efficient manner, holding great promise without any geographical and climatic limitations.[14,15] In this respect, the sorption–desorption cycles facilitated by advanced sorbents are the critical steps in the SAWH process, typically determining their overall freshwater yield and associated energy consumption.[16–19]

To date, numerous state-of-the-art sorbents with high water uptake, rapid kinetics, and energy-efficient regeneration have been developed for SAWH, including various organic frameworks,[20–24] hygroscopic organic liquids,[25] and salt-based composites.[26–29] Among them, hygroscopic salt-hydrogel composites (HSHCs), characterized by confining hygroscopic salts (e.g., lithium chloride (LiCl)) in the hydrogel matrices, have attracted immense attention due to their synergistically enhance the SAWH performance.[30–32] On one hand, the incorporation of salts relieves the issue of slow sorption kinetics for hydrogels,[33–35] while hydrogels, with their swelling property, offer high water retention for enhanced sorption capacity without any leakage risks.[16,19,36] On the other hand, by designing unique molecular structures for hydrogels, their interactions with guest molecules can be efficiently tuned, providing the potential for

**ADVANCED
SCIENCE NEWS**

www.advancedsciencenews.com

**ADVANCED
MATERIALS**

www.advmat.de

higher water uptake[34,35,37] or lower energy demand for water desorption.[38–40] Recently, ongoing efforts in innovating SAWH have led to the development of various emerging HSHCs, including poly[2-(methacryloyloxy) ethyl] dimethyl-(3-sulfopropyl) ammonium hydroxide – LiCl hydrogels (PDMAPS-LiCl),[33,35,41] poly(2-acrylamido-2-methyl-1-propanesulfonic acid – LiCl hydrogels (PAMPS-LiCl),[19] polyacrylamide – LiCl hydrogels (PAM-LiCl),[34,38] and poly(N-isopropyl acrylamide) – LiCl hydrogels (PNIPAM-LiCl),[39,40] all exhibiting remarkable SAWH performance. However, considering the actual demand for SAWH, the sorption/desorption kinetics of these HSHCs remain sluggish, primarily due to inadequate mass transport through the polymer networks.

In recent studies, mechanisms governing SAWH in HSHCs have been unveiled, revealing that sorption/desorption is principally influenced by their vapor transport, surface adsorption, and liquid diffusion.[31,42] Hence, there has been considerable interest in developing different strategies, such as lowering material dimensions and creating open-porous hydrogels, aiming to increase the contact area with vapor and shorten the liquid diffusion distance. For example, converting bulk HSHCs into smaller-sized structures, such as microgels[40,43] and fibers,[44,45] represents a straightforward approach to expanding specific sorption/desorption surfaces, enhancing their SAWH kinetics. Alternatively, aerogels with porous structures created by freezing-drying methods have also been introduced into HSHCs to remarkably accelerate their sorption/desorption rates.[46–49] Unfortunately, this strategy has only been confirmed by systems fabricated from macromolecular polymers, including sodium alginate,[47,50] sodium polyacrylate,[51] and hydroxypropyl cellulose.[52] In these cases, ice crystals merely compel polymer chains to come into proximity with limited interactions, such as hydrogen bonds, electrostatic interactions, and van der Waals forces, which exhibit potential risks of structural failure under various stimuli (e.g., temperature and salt solutions).[53,54] Moreover, increasing the cross-linking contents or the hydrophobicity of material systems may improve the stability of resulting aerogels, but often at the expense of their sacrificing swelling properties, resulting in reduced hygroscopic salt loading and undesirable SAWH performance. Unlike these efforts mainly focus on the construction of pores within their substrates, there has been limited research on the inherent network engineering of hydrogels to enable them with high swelling properties and fast mass transfer capabilities, crucial for the development of HSHCs. In particular, a generalized strategy for typical hydrogel systems used in HSHCs (e.g., PDMAPS, PAM, and PNIPAM), characterized by low-cost, stable covalent networks, and scalable manufacturing characteristics, is essential but rarely explored to improve their sorption/desorption kinetics.

Herein, we present a universal network engineering of hydrogels for HSHCs to significantly enhance their SAWH kinetics. In this concept, a new class of entangled-mesh hydrogels (EMHs) is unprecedentedly developed for HSHCs through a facile cryogelation method. Specifically, the hydrogel precursors were first frozen to form interconnected ice crystals and numerous isolated microdomains before polymerization. Owing to the confinement enrichment effect, the monomers spontaneously aggregated into these microdomains at high concentrations and caused high monomers/water ratios, then initiating polymerization to form

a highly-entangled mesh serviced as the polymeric skeleton. Following the thawing of ice, the EMHs were successfully attained, presenting a distinct interconnected open-macroporous topology (**Figure 1a**). Importantly, this method is also generalized and can be directly applicable to various monomers used in current HSHCs, including zwitterions,[33,35] electrolytes,[19] hydrophilies,[34,38] and phase-change material (PCM) units,[39,40] to prepare the EMHs, offering great material diversity. Compared with the small mesh size ($\xi < 50$ nm) in the conventional dense hydrogels (CDHs) obtained through the regular polymerization, the as-prepared EMHs could create and maintain a stable macroporous topology (pore size (D_v) > 1 µm) due to the formation of numerous highly-entangled mesh confinements featured with restrained swellable properties (Figure 1b). This dissimilarity in the network topology led to an obvious difference in the mass transport properties of the obtained hydrogels. Moreover, the regular homogeneous mesh is retained in the EMHs to link the entangled domains, enabling them with a large swelling property as the CDHs. As a result, the EMHs exhibited more rapid swelling kinetics than the CDHs in both water and LiCl solutions, which confirms that the EMHs possessed higher mass transport properties due to their distinct macroporous topologies (Figure 1c). By embedding hygroscopic LiCl and photothermal graphene oxide (GO) flakes, the hygroscopic EMHs (HEMHs) were achieved and demonstrated both remarkably enhanced sorption and solar-driven desorption kinetics than those of hygroscopic CDHs (HCDHs), in a typical arid climate with low RH of 30% and normal solar intensity of 1.0 sun (Figure 1d). Since these features of the HEMHs, a rapid-cycling harvester prototype was established for practical solar-driven SAWH, delivering a high-yield freshwater production of 2.85 L_{water} $kg_{sorbents}^{-1}$ day^{-1} through continuous eight sorption–desorption cycles, almost higher than the values of the reported HSHCs. In conclusion, this work proposes a novel approach to significantly improve the sorption/desorption kinetics of current HSHCs by adopting a generic network engineering of hydrogels, which holds great promise in addressing the persistent challenges of their slow kinetics, propelling them toward the next-generation SAWH applications (Figure 1e).

2. Results and Discussion

2.1. Fabrication of EMHs Using the Cryogelation Method

Figure 2a illustrates the proposed cryogelation method for engineering a macroporous topology aimed at enhancing their mass transport properties through constructing the highly-entangled mesh confinements within hydrogels. As a proof-of-concept, the zwitterionic PDMAPS hydrogels were selected as the prototypical systems, due to their advantages in SAWH applications, such as high salt loading capability, high sorption capacity, and low salt leakage risk.[33,35] More specifically, the cryogelation method for fabricating the EMHs is divided into two steps, involving solvent crystallization (mainly ice crystals in this work) and confined polymerization. First, the precursor solution was frozen, causing their internal solutes, including monomers, cross-linkers, initiators, and low amounts of water, to spontaneously aggregate into numerous microdomains due to the enrichment effect of ice crystals. Then, these crowed ingredients with high monomers/water
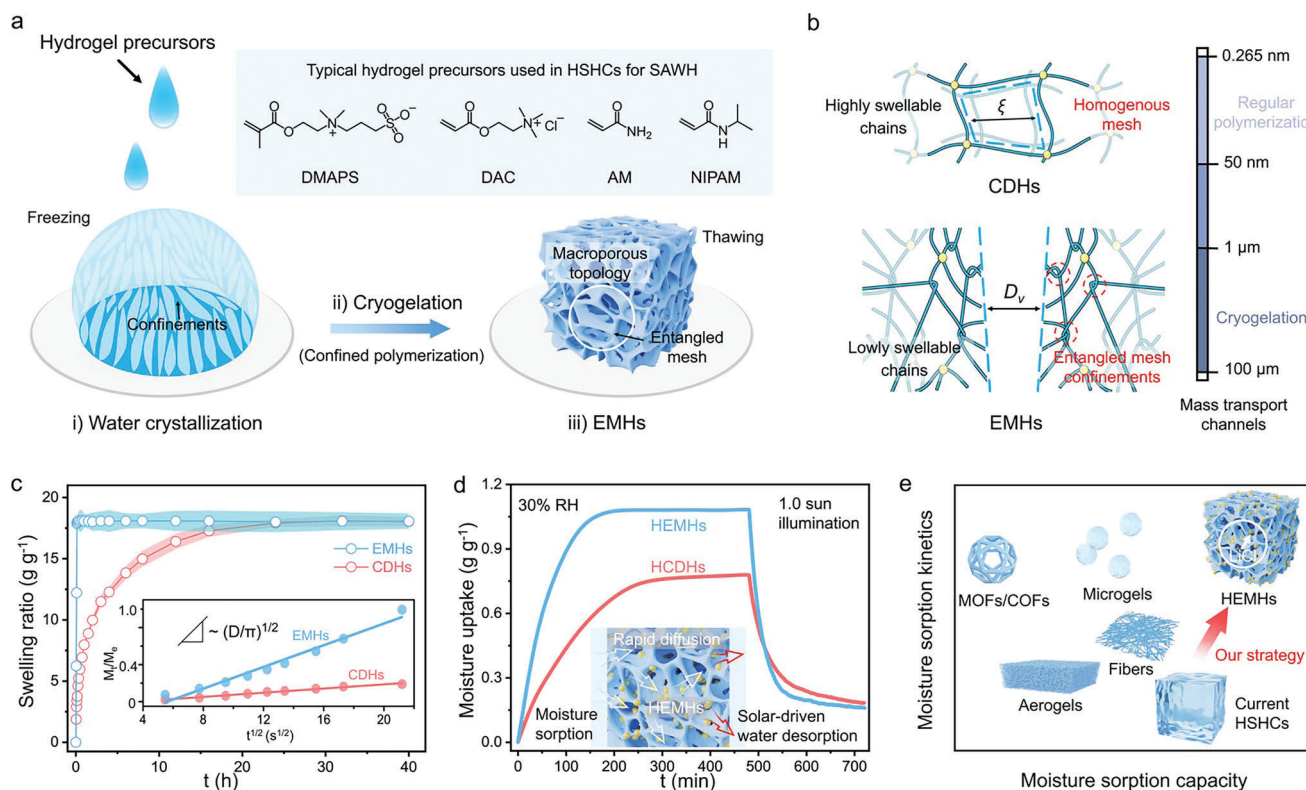
Figure 1. The design concept of network engineering for HSHCs to improve their SAWH kinetics. The EMHs were fabricated using a) the cryogelation method to achieve a macroporous topology within their volumes for higher mass transport properties. Prominent monomers for current HSHCs, including zwitterions (DMAPS), electrolytes ([2-(acryloyloxy) ethyl] trimethylammonium chloride, DAC), hydrophilies (AM), and PCM units (NIPAM), could be utilized to synthesize relevant EMHs through the cryogelation method. b) Schematics of the topological networks of the CDHs fabricated from regular polymerization and the EMHs resulted through the proposed cryogeltaion method, respectively. Typically, the CDHs show small mesh sizes below 50 nm, which is because their homogeneous chains exhibit highly swellable properties upon swelling/deswelling. On the contrary, the EMHs could create and maintain the macroporous topology (D_v over 1 μm), which is attributed to the limited swelling properties of their highly entangled chain confinements. c) Swelling behaviors of the as-prepared EMHs and CDHs in the 10 wt% LiCl solution, where the EMHs displayed faster swelling dynamics and higher mass diffusive coefficients (D). d) Moisture sorption and solar-driven desorption kinetics for the resulting HEMHs and HCDHs at 25 °C, where the moisture sorption at 30% RH and the water desorption under 1.0 sun illumination. e) Schematic comparison of SAWH performances for current state-of-the-art sorbents, demonstrating that our strategy provides a promising solution to address the critical challenge of sorption kinetics for current HSHCs in realizing high-performance SAWH applications.

ratios in the confined microdomains often resulted in crowded polymer mesh that proved to be dense and highly entangled after polymerization.[55] As a result, an obvious phase separation occurred in the as-prepared systems, leading to the formation of a macroporous topology characterized by highly entangled domains linked by homogeneous networks after the ice crystals melted (Figure S1, Supporting Information). Owing to the restrained swellability of the highly-entangled mesh confinements, the resulting macroporous topology within EMHs can be stably preserved during the swelling/deswelling cycles, which is also the key to strengthening their mass transport property.

It was observed that unlike the CDHs obtained from regular polymerization of DMAPS monomers retained a transparent appearance, the resulting EMHs from the same precursors exhibited an opaque one, which originated from their entangled mesh structures caused by cryogelation (Figure S2, Supporting Information). On the other side, the transparent appearance of the CDHs also reflects their homogeneous mesh structure, indicating that their networks are intrinsically highly swellable. Despite

the CDHs exhibiting a porous structure after freezing-drying, the inevitable collapse upon swelling/deswelling potentially induces them into a glassy network due to such high swellable properties of their networks, leading to a significantly declined mass transport performance (Figure S3, Supporting Information). Of note, the EMHs still demonstrated an obvious nonhomogeneous and micrometer-sized macroporous topology after incorporating the GO flakes (Figure 2b).

To visualize this dissimilarity in their network topologies, the corresponding hydrogels upon swelling were characterized. As shown in Figure 2c, a homogeneous network architecture was observed in the hydrated CDHs under confocal laser scanning microscopy (CLSM), clearly indicating the polymer chains in the CDHs were easily collapsed upon swelling. Moreover, the swollen EMHs maintained continuous macroporous structures due to the limited swellable properties of their entangled mesh confinements (Figure 2d). From their X-ray microcomputed tomography (microCT), the EMHs exhibited a 3D continuous inter-connectivity with a measured porosity of ≈76.15%,
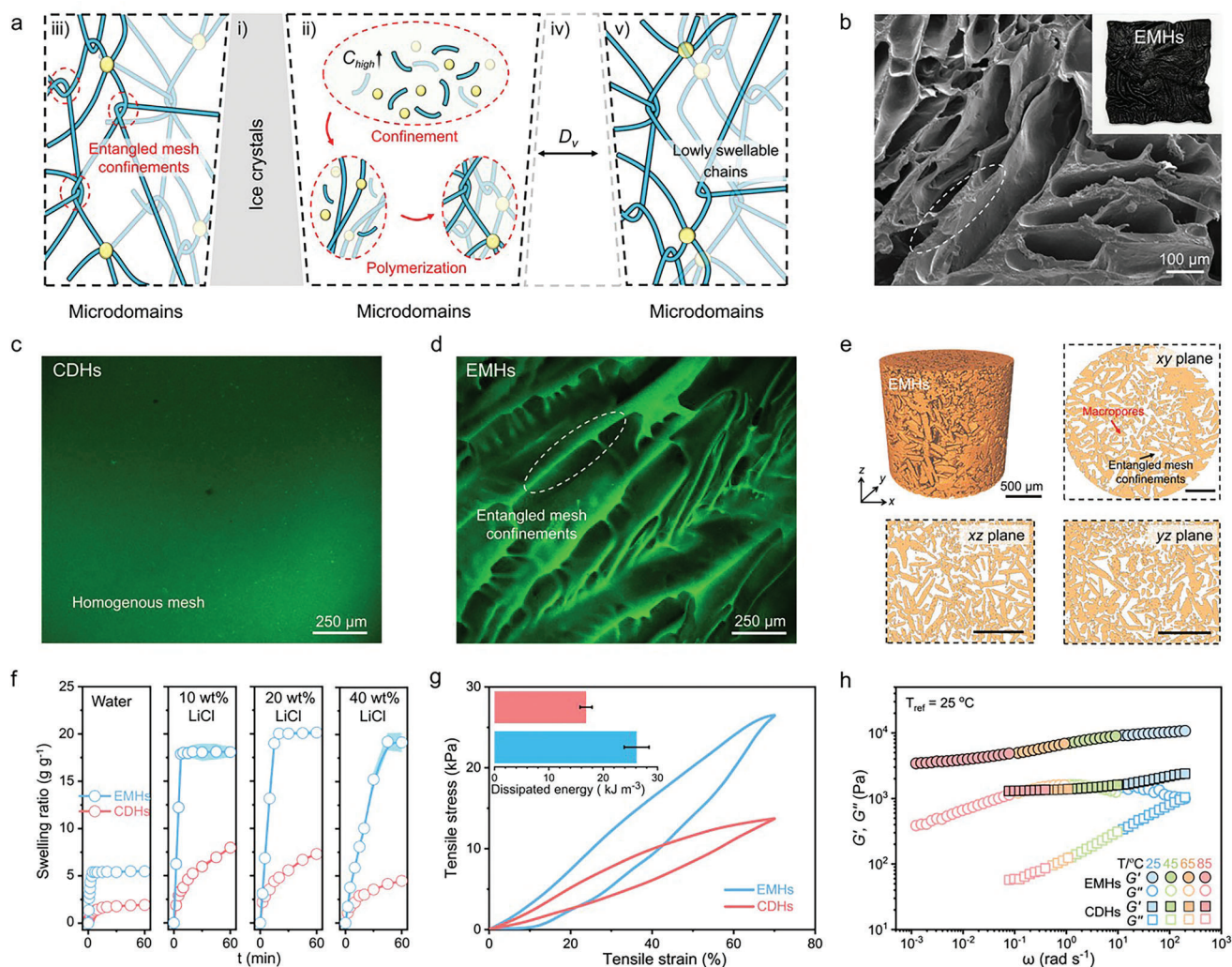
Figure 2. Preparation and characterization of the EMHs used for HSHCs. a) Schematics of the proposed cryogelation method. The EMHs were fabricated by i) first freezing the precursor solution to form ice crystals and isolating numerous microdomains. Then, ii) a confined polymerization was triggered for iii) the generation of a crowed polymer network, which is proven to be highly entangled. iv) After ice crystals thawing, interconnected macroscopic channels (D_v) were presented in the obtained hydrogels. v) Importantly, this macroporous topology can be retained within swelling/deswelling cycles due to the limited swellable properties of their entangled mesh confinements. b) Scanning electron microscope (SEM) images of the obtained EMHs, and the insert shows a photograph of the corresponding hydrogel ($40 \times 40 \times 2$ mm). CLSM images of c) the CDHs with a water content of 2 g g^{-1} and d) the EMHs containing water of 3.5 g g^{-1}, whose colors are derived from the fluorescent components integrated into their polymer networks. e) 3D X-ray microCT images of hydrated EMHs with the water content of 2 g g^{-1}, in which a 3D interconnected macroporous topology was illustrated. The yellow part represents the macropores, while the white region depicts the entangled mesh confinements of the EMHs. The corresponding scale bar is 500 μm. f) Comparison of swelling ratios of the EMHs and CDHs when immersed in water, 10, 20, and 40 wt% LiCl solution within the first hour, respectively. g) Sequential stress–strain cycle of the resulting EMHs and CDHs, respectively, with a comparison of their dissipated energy enabled by their polymer networks in the insert. h) Dynamic mechanical behaviors of the resulting EMHs and CDHs, respectively, in which the master curves for the frequency dependence of G' and G'' at a reference temperature of 25 °C.

which closely aligns with the result obtained from the mercury intrusion method (Figure 2e; and Figure S4, Supporting Information). By contrast, the swollen CDHs only demonstrated a series of nanoscale pores within their volumes, further supporting the idea that porous structures caused by freezing-drying would collapse when water enters them again (Figure S5, Supporting Information). These results are also consistent with their topological morphologies from the CLSM and SEM images. Therefore, it is proved that the confined effect of ice crystals during the polymerization is crucial for forming and maintaining the resulting macroporous topology.

Significantly, these differences in their network topologies resulted in varying swelling properties, particularly for dynamics. As shown in Figure 2f, the developed EMHs exhibited considerably increased swelling rates in diverse solutions. It is worth noting that the EMHs could rapidly reach their swelling equilibrium in just 5, 10, 20, and 45 min in water, 10, 20, and 40 wt% LiCl solutions, respectively, which are greatly faster than

those of the CDHs (Figure S6, Supporting Information). Usually, the swelling kinetics of hydrogel networks are governed by the poroelastic time scale of water diffusion. Thus, the swelling diffusion coefficient (D_{sw}) is a factor reflected in their mass transport performance through the polymer networks.[56] According to Fick's second law model ($M_t/M_e = 2/d \, (Dt/\pi)^{1/2}$, where M_t and M_e are the swollen mass at the given time (t) and equilibrium for swollen process, respectively, and d is the thickness of dry hydrogel, ≈1 mm), corresponding D_{sw} values of the hydrogels were obtained through plotting the normalized weight (M_t/M_e) by against the square root of t ($t^{1/2}$) (Figure S7, Supporting Information). For the CDHs, lower D_{sw} values in various solutions were attributed to their dense polymeric networks, largely restricting the mass diffusion within their volume. In contrast, the obtained EMHs demonstrated a boosted water swollen property (higher D_{sw} values), which is possible due to their unique entanglement-enabled macroporous topology: 1) the interconnected macroporous topological structures are stable enough even after swelling due to their inner entangled mesh confinements featured with limited swellable properties, 2) the macroscopic pore diameter (9–178 µm) ensures a large unconfined space for water diffusion and swollen, 3) the macroporous geometry offers absorbed water molecules with more accessible absorption sites and shorter transport distance in the glassy volume of hydrogels, both leading to an increasing probability of water diffusion. It is worth noting that the EMHs demonstrate the ability to repeat this rapid swelling for up to 10 cycles (Figure S8, Supporting Information). Even after immersion in LiCl solution for eight months, the swelling properties of the EMHs showed no obvious reductions, indicating the excellent stability of their inner macroporous topologies (Figure S9, Supporting Information).

In addition, a comparative experiment was conducted to further visualize their enhanced mass transport, where paper tapes were utilized as water absorbents, and the corresponding performance was reflected in the transport height, as schemed in Figure S10 (Supporting Information). As observed, the water transport height of the EMHs reached 5.05 cm, comparable to that of direct immersion of the paper tape in water, demonstrating their excellent mass transport performance. Analogous results were successfully observed in the other three hydrogel systems, including PDAC, PAM, and PNIPAM, all of which are typical hydrogels used in current HSHCs (Figures S11–S14, Supporting Information). This confirms the broad applicability of the presented cryogelation method for the preparation of hydrophilic hydrogels starting from monomers to boost their mass transport properties.

In order to reveal their network structures, the mechanical properties of the EMHs were examined and analyzed. From their stress–strain curves, the EMHs displayed higher stiffness and lower stretchability than those of the CDHs, suggesting there are more cross-linking sites within the EMHs (Figure S15, Supporting Information). This could be attributed to the forced sliding of the entangled polymer chains, allowing the transfer of force along the polymer chains and avoiding the fracture of weak chains.[55,57] Moreover, a broader hysteresis loop was observed in the loading/unloading cycle of the EMHs compared with the CDHs, which suggests a larger energy dissipation (26.1 kJ m^{-3}) provided by relevant movements of highly-entangled mesh structures (Figure 2g). Furthermore, the master curves of EMHs

and CDHs at a reference temperature of 25 °C were obtained using the time-temperature superposition (TTS). As shown in Figure 2h; and Figure S16 (Supporting Information), a rubbery region with storage modulus (G') > loss modulus (G'') could be observed from the master curves of the EMHs and CDHs in a wide frequency range of 10^{-3}–10^2 rad s^{-1}, suggesting their elastic and stable cross-linked networks.[58,59] In this process, the EMHs demonstrated a higher G' value of 3.50 kPa compared to that of the CDHs (1.35 kPa), revealing their greater cross-linking degree resulted from the interchain entanglements aggregated in microdomains.[60] Meanwhile, the EMHs also exhibited a larger loss factor (tan δ) compared to the CDHs, indicating their higher energy dissipation ability,[61] which was in good agreement with previous stretching-relaxation data (Figure S17, Supporting Information). Remarkably, the entanglements within the EMHs could be efficiently manipulated through tuning monomer concentrations in their precursors. As shown in Figures S18 and S19 (Supporting Information), a rising entangled degree of the resulting EMHs was observed as their monomer concentrations increased from 4.48×10^{-4} to 1.79×10^{-3} mol cm^{-3}, accompanied by enhanced energy dissipation and decreased equilibrium swelling, consistent with previous findings on entangled polymeric networks.[55,62] Accordingly, these results confirmed that an expected network with a high degree of entanglements was successfully attained in the resulting EMHs.

In short, such a strategy for a stable macroporous topology highly facilitates mass transport properties for hydrogels compared to the regular methods, which shows great potential to accelerate their sorption/desorption processes. Subsequently, through a facile immersing-drying method, the hygroscopic LiCl is controllably integrated into the as-prepared hydrogels, preparing the HEMHs and HCDHs for SAWH applications.

2.2. Moisture Sorption Performance Evaluation

As reported, the LiCl contents in the HSHCs played a critical role in their moisture sorption capacity. Thus, the optimized LiCl content in the resulting HEMHs was first explored for desirable SAWH performance. To this end, the HEMHs with LiCl mass fractions ranging from 5 to 85 wt% were prepared by swelling in various concentrations of LiCl solutions. As shown in Figure S20 (Supporting Information), the equilibrium sorption capacity (ESC) of the as-prepared HEMHs demonstrated a rising trend as the LiCl contents increased. However, the HEMHs with 85 wt% (termed as HEMHs-85%) showed slower kinetics compared to the HEMHs-65% with the closed ESCs. This is because, while excess LiCl could enhance their ESC, it also resulted in their inevitable aggregation, leading to restricted mass transport and thus exhibiting slow kinetics in the early stages.[34,38] As such, the HEMHs-65% were chosen for the following comparison with the corresponding HCDHs, where they contained identical LiCl contents of 65 wt% (Figure S21, Supporting Information).

Remarkably, significant volume enlargements were observed for both the as-prepared HEMHs and HCDHs after moisture sorption at 25 °C and 30% RH for 8 h, with the area of HEMHs increasing by ≈31% more than that of HCDHs, attributed to their larger porous topologies (Figures S22 and S23, Supporting Information). The dynamic sorption curves in three typical climate

ADVANCED
SCIENCE NEWS

www.advancedsciencenews.com

ADVANCED
MATERIALS

www.advmat.de
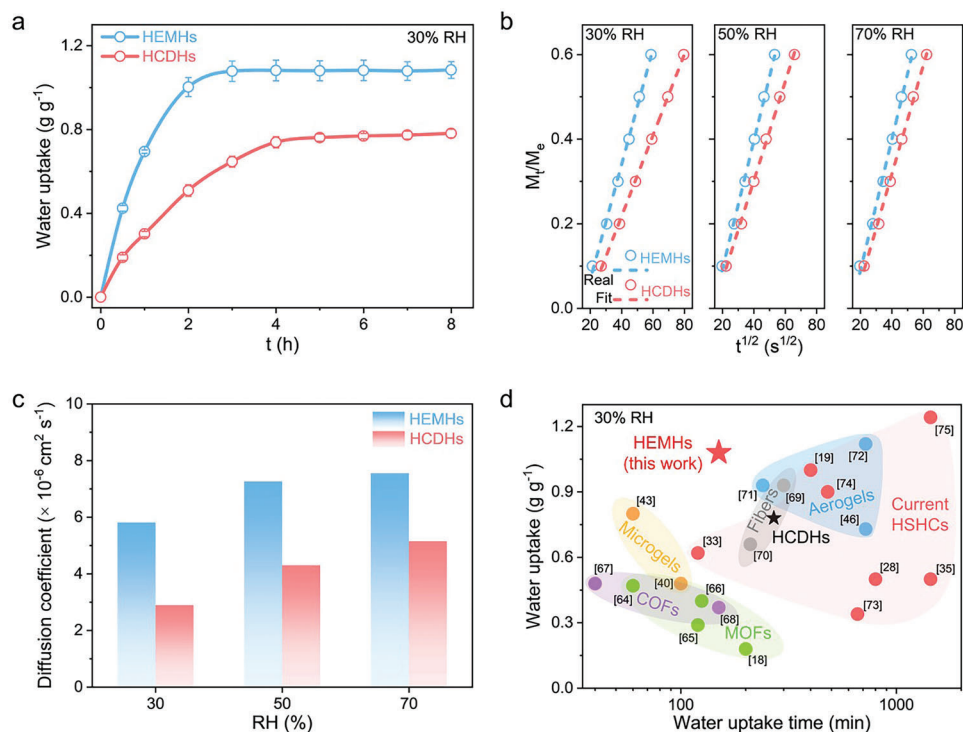
Figure 3. Moisture sorption performance evaluation. a) Moisture sorption kinetics curves of the HEMHs and HCDHs at 30% RH and 25 °C. b) Normalized sorption ratios (M_t/M_e) were plotted as the function of $t^{1/2}$ based on the results in (a), where the spheres represent the experiment data and the lines are fitted data by Fick's second law. c) The calculated D_{ms} values of the HEMHs and HCDHs at 30%, 50%, and 70% RH, respectively. d) Comparison of sorption kinetics with other state-of-the-art sorbents at 30% RH, including MOFs,[18,64–66] COFs,[67,68] fibers,[69,70] microgels,[40,43] aerogels,[46,71,72] and current HSHCs.[19,28,33,35,73–75]

conditions of the arid regions (30%, 50%, and 70% RH) were illustrated in **Figure** 3a; and Figure S24 (Supporting Information). In contrast to the HCDHs, the HEMHs were found to realize enhanced kinetics, achieving the ESCs of 1.08, 1.52, and 2.36 g g^{-1} within 150, 200, and 240 min at the RHs of 30%, 50%, and 70%, respectively. Whereas, the HCDHs required more sorption time to reach their ESCs under the same conditions and exhibited reduced ESCs of 0.78, 1.21, and 1.90 g g^{-1} with equilibrium times of 270, 290, and 320 min, respectively. The moisture sorption diffusion coefficient (D_{ms}), representing the sorption rate, can be estimated by Fick's second law (Figure 3b). As expected, an ideal linear fitting between the experimental data and the proposed theoretical mode was observed at different RHs and 25 °C (Table S2, Supporting Information). The corresponding D_{ms} values are summarized in Figure 3c. From the results, the HEMHs exhibited higher D_{ms} values, reaching 5.81×10^{-6}, 7.26×10^{-6}, and 7.55×10^{-6} cm^2 s^{-1} at 30%, 50%, and 70% RH, respectively, while the HCDHs achieved only 2.89×10^{-6}, 4.30×10^{-6}, and 5.15×10^{-6} cm^2 s^{-1} at the same RHs. Of note, the resulting HEMHs could maintain the superiority sorption performance without leakage even after moisture sorption in 90% RH for 12 h, demonstrating the excellent cyclic stability and rapid sorption rates (Figure S25, Supporting Information).

Moreover, the moisture sorption isotherms of HEMHs and HCHDs were performed at 30% RH to assess their corresponding ESCs at varying temperatures. As shown in Figure S26 (Supporting Information), the HEMHs reached the ESCs of 1.12,

1.08, and 1.00 g g^{-1} at 15, 25, and 35 °C, respectively, significantly higher than that of HCDHs. Additionally, the relevant water sorption enthalpies (ΔH_{sorp}) were calculated from the water sorption isotherms at different temperatures.[63] As shown in Figure S27 (Supporting Information), the ΔH_{sorp} values of HEMHs were estimated to be −2818 to −2537 J g^{-1} as their water contents increased from 1.2 to 3.5 g g^{-1}, according to the Clausius–Clapeyron equation. By contrast, the ΔH_{sorp} values of HCDHs increased, ranging from −2874 to −2553 J g^{-1}, under the same conditions, which suggests that the hydrated HCDHs required more energy input for water desorption and will be discussed in detail in Section 2.3.

As a result, benefitting from their enhanced mass transport properties caused by their robust macroporous topologies, the HEMHs delivered a significantly improved moisture sorption performance than the regular HCDHs, particularly for kinetics. As observed in Figure 3d, the HEMHs achieved an impressive ESC of 1.08 g g^{-1} within 150 min, which is almost double that of the HCDHs in this work (only 0.78 g g^{-1} for 270 min) and is also prior to the values reported by other state-of-the-art sorbents (Table S3, Supporting Information).

2.3. Solar-Driven Water Desorption Performance Evaluation

Water desorption is another crucial step in SAWH, as it determines the ultimate freshwater yield and plays a vital role in

**ADVANCED
SCIENCE NEWS**

www.advancedsciencenews.com

**ADVANCED
MATERIALS**

www.advmat.de
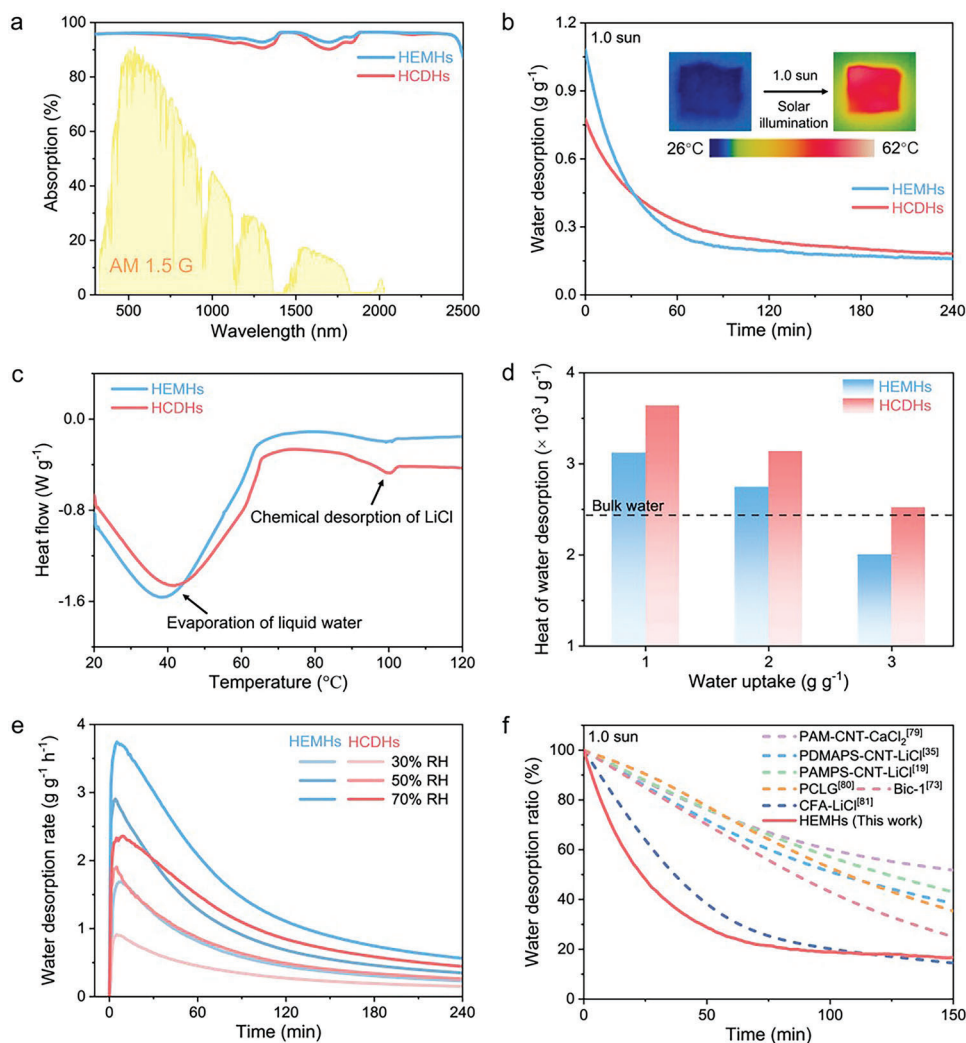
Figure 4. Solar-driven water desorption performance evaluation. a) Solar absorption spectra of the hydrated HEMHs and HCDHs, respectively. The yellow shadow is the solar spectral irradiance weighted by the standard AM 1.5 G solar spectrum. b) Water desorption kinetics curves of HEMHs and HCDHs at 1.0 sun solar illuminations. Inset shows the IR photos of the HEMHs hydrated in 30% RH for 8 h before and after 1.0 sun solar illumination for 240 min. c) Heat flow curves of HEMHs and HCDHs with the same water content of 3 g g^{-1} during the water evaporation process measured by DSC. d) ΔH_{desp} values of HEMHs and HCDHs with different water uptake. e) Water desorption rates of HEMHs and HCDHs that were hydrated at 30%, 50%, and 70% RH for 8 h under 1.0 sun solar illumination. f) Comparison of water desorption behaviors in the first 150 min, under 1.0 sun solar illumination.[19,35,73,79–81]

their regenerated hygroscopicity. Given the ubiquity and abundance of natural solar energy, solar-driven water desorption is anticipated to offer an environmentally friendly, cost-effective, and sustainable alternative for extracting water from hydrated sorbents.[46,47] In this case, the rational incorporation of hydrophilic GO flakes endows the as-prepared hygroscopic systems with considerable photothermal properties, ensuring sufficient heat input for the desorption of absorbed water. **Figure 4a** suggests that the HEMHs and HCDHs achieve approaching and high-efficient solar absorption of 96.24% (from 300 to 2500 nm). Under one sun illumination, the surface temperatures of the HEMHs and HCDHs showed identical changes, rapidly increasing in the first 15 min and then reaching equilibrium at ≈53.4 and 52.1 °C, respectively (Figure S28, Supporting Information). Similar temperature trends were also observed under 0.7 sun and

1.5 sun illumination, indicating that these two resulted systems are capable of superior photo-to-thermal conversion to realize high-efficient solar-driven water evaporation (Figure S29, Supporting Information).

Then, their solar-driven water desorption performance was evaluated under solar illumination with varying intensities (from 0.7 to 1.5 sun). As shown in Figure 4b; and Figure S30 (Supporting Information), all tested hydrogels that were hydrated in 30% RH for 8 h experienced significant water release and rapidly reached equilibrium. Of note, the hydrated HEMHs achieved ≈76%, 85%, and 91% of water desorption within 140, 120, and 70 min under solar illumination of 0.7, 1.0, and 1.5 suns, respectively, outperforming the HCDHs with 59%, 74%, and 81% desorption under the same conditions. These results proved that the HEMHs deliver higher water

**ADVANCED
SCIENCE NEWS**
www.advancedsciencenews.com

**ADVANCED
MATERIALS**
www.advmat.de

desorption kinetics than the HCDHs. Analogous to moisture sorption evaluation, the water desorption diffusion coefficient (D_{wd}) was also calculated to reflect their desorption rates using Fick's second law, as follows: $(X_t - X_e)/(X_0 - X_e) = 1 - 2/d (Dt/\pi)^{1/2}$, where X_0, X_t, and X_e are the initial mass, the water content at given time (t) and equilibrium for desorption process, respectively, and d is the hydrogel thickness. As expected, the HEMHs were estimated with considerable D_{wd} values and reached 11.22×10^{-6}, 12.69×10^{-6}, and 29.42×10^{-6} cm^2 s^{-1} when expose to solar illumination of 0.7, 1.0, and 1.5 suns, respectively (Figure S31 and Table S4, Supporting Information). In contrast, the D_{wd} values of the HCDHs under identical solar intensities were only 7.07×10^{-6}, 7.55×10^{-6}, and 19.01×10^{-6} cm^2 s^{-1}, respectively. Thus, the HEMHs with higher D_{wd} values are considered to have faster water desorption kinetics.

In order to shed light on the enhanced water desorption capabilities, it is necessary to explore the corresponding desorption heat (ΔH_{desp}) of the obtained hydrated hydrogels. The different scanning calorimetry (DSC) results showed two same evaporation peaks appeared in the curves of the hydrated HEMHs and HCDHs, corresponding to the evaporation of liquid water and the chemical desorption of LiCl[38] (Figure 4c; and Figure S32, Supporting Information). Though integrating the heat flow over time, the ΔH_{desp} values under various stages with different water contents were computed. As shown in Figure 4d, the HEMHs showed low ΔH_{desp} values of 3122, 2645, and 2004 J g^{-1} at water content of 1, 2, and 3 g g^{-1}, respectively. In comparison, the HCDHs exhibited higher ΔH_{desp} values, reaching up to 3641, 3140, and 2521 J g^{-1}, respectively. Therefore, the HEMHs presented a lower desorption barrier ($\approx$500 J g^{-1}), offering the potential for faster desorption kinetics under the same heat input. This analysis is also consistent with the previous conclusions regarding the sorption heat.

Further studying of the water states within their volumes reveals significant differences in the resulting HEMHs and HCDHs. In general, the water molecules absorbed in the hydrogels can be classified into three types, including bound water, intermediate water, and free water, based on their interaction strengths with other substances (e.g., polymer networks and salts).[76,77] Among them, bound water, referring to the water molecules captured by the host's hydrophilic sites through strong interactions (e.g., hydrogen bonding), requires more energy to release during evaporation. Conversely, intermediate and free water demonstrate relatively lower energy demands for desorption due to their weaker interactions. In DSC melting tests, the bound water tends to be nonfreezable due to their strong interactions with the substances, while the other two water molecules present typical freezable properties below 0 °C, from which their contents can be estimated.[78] As a result, the hydrated HEMHs exhibited higher freezable water contents of 0.16, 0.81, and 1.62 g g^{-1} than those of the hydrated HCDHs (0.05, 0.68, and 1.38 g g^{-1}) when their water contents were 1, 2, and 3 g g^{-1}, respectively (Figure S33 and Table S5, Supporting Information). This indicates that there was less bound water in the hydrated HEMHs compared to the HCDHs, which could reduce the energy demand ΔH_{desp} for water desorption. Note that this result can be attributed to the greater opportunity for the water molecules to interact with the hydrophilic polymer chains in the HCDHs due to the high swelling behaviors of their homogenous chains, thus increasing

their bound water amount. In contrast, absorbed water molecules mainly accumulate in the volume excluded due to the formation of abundant entangled mesh confinements within the HEMHs, of which bound water only accounts for a small fraction.

As a result, the HEMHs with various water contents all exhibited faster desorption rates than the HCDHs due to the reduced desorption barrier (Figure 4e; and Figure S34, Supporting Information). Specifically, the HEMHs hydrated with 30%, 50%, and 70% RH achieved the maximum water release rates of 1.69, 2.91, and 3.74 g g^{-1} h^{-1} under 1.0 sun illumination, respectively. These values were remarkably higher than the maximum desorption rates of 0.91, 1.91, and 2.36 g g^{-1} h^{-1}, observed in the hydrated HCDHs. Moreover, a comparison with previously reported hydrogel-based sorbents on solar-driven water desorption kinetics is summarized in Figure 4f; and Table S6 (Supporting Information). The results indicated that the resulting HEMHs facilitated a leading water release rate (equilibrium time of 120 min) and greater desorption ratio (85%) under one sun solar illumination, thereby being expected to realize more high-efficient SAWH performance.

2.4. Outdoor Experiments for Solar-Driven SAWH

Apart from sorption/desorption performance, the long-term stability of the HSHCs is also a prerequisite for practical SAWH applications. As shown in **Figure 5a**, the HEMHs are capable of keeping good performance retentions after multiple sorption–desorption cycles, showing stable equilibrium and dynamic characteristics. After experiencing a cycle containing 35 min of moisture sorption and 25 min of water desorption, the HEMHs could deliver a high-yield freshwater generation of 0.37 g g^{-1} in a typical arid climate (30% RH, 25 °C and 1.0 sun illumination), indicating their immense potential for practical SAWH applications (Figure 5b). Thus, integrating such HEMHs on a large scale was of great interest and then explored (Figure S35, Supporting Information). However, the mismatch between relatively low moisture sorption and fast desorption rates remains challenging to realize high-efficient practical freshwater extraction from the air. To address this issue, recent studies have proven that continuous multiple harvesting is rational for improving their daily freshwater yield, which makes full use of the high RH conditions during nighttime and further optimizes multiple sorption/desorption cycles throughout the daytime.[17,19,51] In this regard, the rapid sorption/desorption kinetics is one of the most critical parameters for these sorbents. As such, the obtained HEMHs in this work are anticipated to be desirable for all-day multicyclic SWAH applications, with their enhanced sorption/desorption kinetics.

To demonstrate their practical water harvesting potential, a self-made modularized harvester based on the obtained HEMHs was engineered, including a moisture distributor, a water desorption chamber, a switchable baffle, an environment monitor, a freshwater collector, and a solar cell module (Figure 5c,d). In the sorption stage, an electric fan driven by electricity harvested by a solar cell was used to distribute the moisture to accelerate the moisture sorption of the HEMHs. Also, during the desorption process, the hydrated HEMHs were exposed to sunlight to evaporate the absorbed water, which then condensed into a water flow and was collected by the water reservoirs. Notably, by

**ADVANCED
SCIENCE NEWS**

www.advancedsciencenews.com

**ADVANCED
MATERIALS**

www.advmat.de
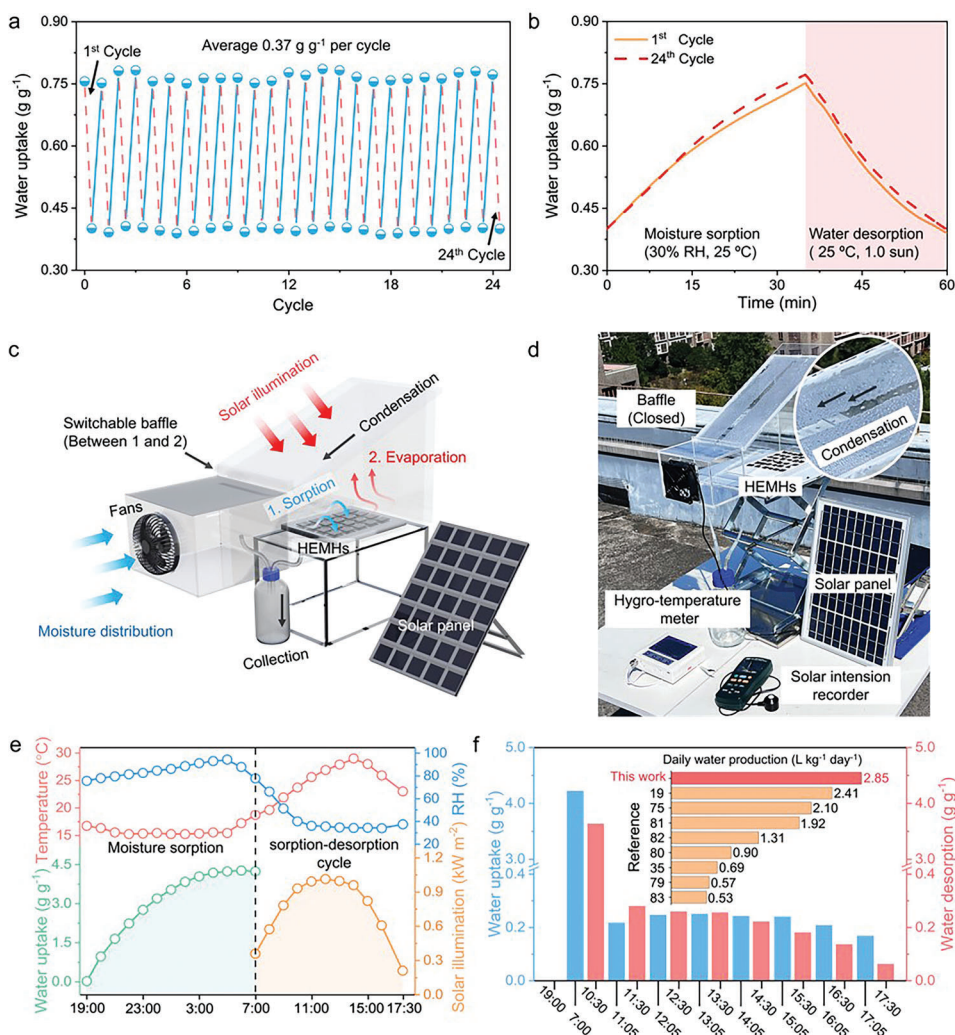
Figure 5. Outdoor SAWH experiments of the resulting HEMHs. a) Cycling performance of HEMHs, where moisture sorption occurred at 30% RH, 25 °C, and water desorption was conducted under 1.0 sun solar illumination in the lab. Each cycle took 1 h, for a total of 24 cycles per day. b) Sorption–desorption curves of HEMHs at cycle 1 and cycle 24, demonstrating their rapid kinetics and cyclic stability. c) Schematic of the self-made modularized harvester based on the resulting HEMHs for practical SAWH. d) Photograph of the solar-driven water desorption of the actual HEMHs-based harvester under natural solar illumination. e) The changes in environmental conditions, including RH, temperature and solar illumination, and water uptake, were recorded for the outdoor SAWH experiment. f) The variation of water uptake throughout the outdoor experiments. Insert shows the comparison of the daily water production with other state-of-the-art hydrogel-based sorbents.[19,35,75,79–83]

removing/putting into the switchable baffle, this system could easily be tuned between moisture sorption and water desorption to achieve a continuous multicyclic SAWH. As a result, such a harvester capable of continuous multicyclic sorption/desorption was implemented for practical freshwater generation in Ningbo, China, from 19:00 on May 22 to 17:30 on May 23, 2023 (Figure 5e). After 12 h of exposure to an average temperature of 15.8 °C and an average RH of 85.4% at night, the dried HEMHs (5.01 g) achieved a prominent moisture uptake of 4.23 g g^{-1} (Figure S36, Supporting Information). Afterward, the baffle was inserted into the harvesting system to form a hermetic space for solar-driven water desorption. Due to their excellent photothermal properties, the surface temperature of the hydrated HEMHs could rapidly increase to 43.4 °C when exposed to natural sunlight (Figure S37, Supporting Information). Con-

sequently, a fast water release of 3.64 g g^{-1} was realized for the hydrated HEMHs within 3.5 h. Since most of the absorbed water was removed, the HEMHs then underwent successive multicyclic sorption and desorption (from 10:30 to 17:30) to increase their daily freshwater production. It was found that seven cycles could be completed within 7 h, and each cycle consisted of a 35 min moisture sorption and 25 min water desorption. As such, this rapid-cycling harvester achieved an unprecedented freshwater production of 2.85 L kg^{-1} day^{-1}, outperforming the state-of-the-art hydrogel-based sorbents for SAWH (Figure 5f; and Table S7, Supporting Information).

Additionally, the energy conversion efficiency (η) of the HEMHs-based device in practical solar-driven water desorption was calculated to be 39.2% (Figure S1, Supporting Information). Moreover, the concentrations of various residual ions,

**ADVANCED
SCIENCE NEWS**

www.advancedsciencenews.com

**ADVANCED
MATERIALS**

www.advmat.de

including Na^+, K^+, Ca^{2+}, and Mg^{2+}, in the water collected by this system were analyzed by an inductively coupled plasma mass spectrometry (ICP-MS). The results showed that all ion concentrations completely comply with WHO drinking water standards (Figure S38, Supporting Information). Overall, by comparing with other state-of-the-art sorbents in terms of moisture uptake, sorption/desorption kinetics, cyclability, and practicability, the HEMHs demonstrated their superiority with all these critical requirements for practical SAWH, thus demonstrating considerable competitive (Figure S39, Tables S8 and S9, Supporting Information).

3. Conclusion

To conclude, we demonstrated a universal network engineering to develop a new class of EMHs with distinct macroporous topologies through a cryogelation for HSHCs, proving a success in substantially improving their SAWH kinetics. This innovative strategy was successfully validated by the PDMAPS-based HSHCs to significantly promote their sorption and solar-driven water desorption kinetics. Benefitting from their stable macroporous topologies enabled by their highly-entangled mesh confinements, the EMHs exhibited considerably improved mass transport properties compared with the CDHs obtained from regular polymerization, which could achieve faster swelling dynamics in both water and LiCl solutions. As a result, the corresponding HEMHs realized impressive moisture sorption kinetics at 30% RH (1.08 g g^{-1} within 150 min), which was more rapid than the regular HCDHs (0.78 g g^{-1} for 270 min). Moreover, the resulting HEMHs presented more rapid solar-driven water desorption behaviors due to the declined desorption heat caused by their distinct macroporous topologies. Finally, a rapid-cycling HEMHs-based harvester was capable of a recorded freshwater yield of 2.85 L$_{water}$ kg$_{sorbents}^{-1}$ day^{-1} through a continuous eight sorption/desorption cycles, outperforming the state-of-the-art hydrogel-based sorbents. Notably, the proposed strategy, based on engineering generic polymer networks, can be easily imparted to other typical hydrogels used for HSHCs. This work paves the way to efficiently improve the sluggish sorption/desorption kinetics of current HSHCs, which is a long-standing challenge for them to realize high-performance SAWH applications. Significantly, this generic network engineering approach for hydrogel candidates also holds great promise in various emerging applications, including water desalination, catalysis, and ion batteries, given its potential to boost their mass transport properties.

4. Experimental Section

Materials: [2-(methacryloyloxy)ethyl] dimethyl-(3-sulfopropyl) ammonium hydroxide (DMAPS), acrylamide (AM), *N,N′*-methylenebis(acrylamide) (BIS), ammonium persulfate (APS), *N,N,N′,N′*-tetramethylethylenediamine (TEMED), lithium chloride (LiCl) were purchased from Aladdin Shanghai Reagent Co., Ltd., *N*-isopropyl acrylamide (NIPAM) was obtained from TCI Shanghai Co., Ltd., [2-(acryloyloxy) ethyl] trimethylammonium chloride (DAC, 80 wt% in water) was provided from Macklin Shanghai Reagent Co., Ltd. All the chemicals were analytical grades and used as received. Graphene oxide (GO) slurry (7 wt% in water) was self-made using a modified Hummers method.

Fabrication of the EMHs by the Cryogelation Method: In a typical synthesis, DMAPS monomers (2.0 g), BIS (0.01 g), and TEMED (20 µL) were dissolved in 8.0 mL deionized (DI) water via ultrasonication for 5 min to obtain a clear and transparent solution. Then, the initiator APS (0.02 g) was dissolved into the resulting solution, and residual oxygen gas was removed by continuously blowing nitrogen gas for 10 min. Subsequently, the precursor solution was encapsulated into a self-made mold with a thickness of 2 mm, sealed, and frozen at −20 °C for 2.0 h. After completely frozen, the precursor solution was quickly transferred to a refrigerator at −5 °C for an in situ polymerization of 12 h. Finally, the as-synthesized hydrogels were melted at room temperature and then immersed in DI water for 48 h to remove unreacted materials. Eventually, the EMHs were obtained. To introduce the photothermal property to the polymer network, the GO slurry (0.4 g) was dispersed in the above precursor before being frozen. Notably, this strategy can apply to other monomers, such as DAC, NIPAM, and AM, for the EMHs through the same processes described above. The detailed synthesis conditions are summarized in Table S1 (Supporting Information). Furthermore, as the comparative samples, the CDHs were synthesized by regular polymerization, where the same precursor solution was directly polymerized without a frozen process.

Fabrication of the HEMHs: A most reported immersing-drying method was employed to enable the resulted hydrogel hygroscopicity for SAWH. In a typical synthesis, the purified EMHs were firstly dried in an oven of 70 °C for 12 h to release inner water completely. Then, the dried EMHs were immersed into a 10 wt% LiCl solution (16 mL) for 48 h at 25 °C to obtain the swollen ones. The mass changes of the resulted hydrogels during the swelling process were monitored until the set values. Finally, the HEMHs were achieved through a complete water desorption at 90 °C. Various concentrations of LiCl solutions, including 5, 10, 20, 40, and 60 wt%, were applied to develop the HEMHs with different salt contents. Also, the HCDHs were realized by the methods described above.

Material Characterizations: The morphologies after freezing-drying were examined by SEM (S4800, Hitachi) at an acceleration voltage of 10 kV. The in-situ swollen morphologies were revealed by confocal laser scanning microscopy (TCS SPS, LEICA) with an excitation wavelength of 405 nm, where a hydrophilic monomer (4-(2-dimethylaminoethyloxy)-*N*-allyl-1,8-naphthalimide) was copolymerized into the tested hydrogels for observation. The 3D macrostructure analyses were performed in a Zeiss Xradia 610 Versa 3D microCT with a voltage of 80 kV and a power of 10 W. The obtained images were reconstructed by Carl Zeiss's Object Research Systems (ORS) image analysis program. The porosity and pore size were characterized by a mercury porosimeter (Autopore IV 9500, Micromeritics). The tensile measurements were tested using a universal material testing machine of 1.0 kN (Z1.0, Zwick). The rheological characterizations were conducted by a Haake MARSIII rheometer (HR-3, TA) equipped with a geometry of 25 mm parallel plates. The LiCl contents of samples were tested by a thermogravimetric analyzer (TG209F1, Netzsch) with a ramping rate of 20 K min^{-1} in air. The melting and evaporation behaviors of samples were tested by a differential scanning calorimeter (DSC 214, Netzsch). Both the melting and evaporation curves were tested in a nitrogen atmosphere at a flow rate of 40 mL min^{-1} and the ramping rate of 5 and 2 K min^{-1} for melting and evaporation, respectively. The solar absorption spectra were performed by an ultraviolet–visible–near-infrared spectrophotometer equipped with an integrating sphere (Lambda 950, Perkin-Elmer). Moisture sorption performance was evaluated by a temperature-and-humidity chamber (SMC-80-CB-2, SANWOOD, with high-temperature uniformity (less than ± 0.5% °C) and high humidity uniformity (less than ± 1.5% RH). The solar-driven water desorption was conducted by a solar simulator (HM-Xe 500 W) equipped with an AM 1.5 G filter. The residue concentrations of ions in the collected water samples were analyzed using an inductively coupled plasma mass spectrometry (ICP-MS, NexION 300X).

The Swelling Experiments: The hydrogels were dried at 70 °C to completely release inner water before swelling. All swelling tests were conducted at 25 °C. Relevant swelling ratio (M) can be estimated from the gain weight (Δm) after immersing in the solution and their dry weight (m_0) and is given by ($M = \Delta m / m_0$). The equilibrium was achieved when the mass change was less than 0.05 wt% in the three consecutive records.

**ADVANCED
SCIENCE NEWS**

www.advancedsciencenews.com

**ADVANCED
MATERIALS**

www.advmat.de

Moisture Sorption and Desorption Experiments: Moisture sorption and water desorption performance can be evaluated by the mass change by an electrical balance (ME204E, METTLER, 0.1 mg). Moisture sorption was measured under constant temperatures and humidities. The initial sizes of the tested samples in this work were set as $9 \times 9 \times 2$ mm and predried at 90 °C for 48 h before use. The sorption kinetics experiments were measured at 25 °C and different RHs (30%, 50%, and 70% RH) for 8 h, and the sorption isotherms were assessed at different temperatures (15, 25, and 35 °C). The desorption experiments were conducted by the solar simulator, and the relevant temperature changes were recorded by an infrared camera (Optris pi 400). For cyclic sorption/desorption experiments, the samples were first absorbed at 30% RH, 25 °C for 35 min, then desorbed under 1.0 sun solar illumination for 25 min in every cycle. All the indoor experiments were tested in the lab with a constant temperature of 25 °C and 30% RH. In the outdoor SAWH experiment, the ambient temperature and humidity were monitored by an automatic temperature-and-humidity sensor (varied by ± 0.1 °C and ± 2.0% RH), and the actual solar illumination was recorded by a portable light intensity meter (DT-1307, CEM, ± 10 W m^{-2}).

Supporting Information

Supporting Information is available from the Wiley Online Library or from the author.

Conflict of Interest

The authors declare no conflict of interest.

Data Availability Statement

The data that support the findings of this study are available from the corresponding author upon reasonable request.

[1] F. Sultana, *Water Int.* **2018**, *43*, 483.
[2] P. H. Gleick, *Water in Crisis: A Guide to the World's Fresh Water Resources*, Oxford University Press, New York **1993**.
[3] M. M. Mekonnen, A. Y. Hoekstra, *Sci. Adv.* **2016**, *2*, e1500323.
[4] C. J. Vörösmarty, P. Green, J. Salisbury, R. B. Lammers, *Science* **2000**, *289*, 284.
[5] R. F. Service, *Science* **2006**, *313*, 1088.
[6] World Meteorological Organization, State of Global Water Resources 2022, https://wmo.int/publication-series/state-of-global-water-resources-2022 (accessed: October 2023).
[7] C. He, Z. Liu, J. Wu, X. Pan, Z. Fang, J. Li, B. A. Bryan, *Nat. Commun.* **2021**, *12*, 4667.
[8] United Nations, Revision of World Urbanization Prospects, https://population.un.org/wup/ (accessed: May 2018).
[9] J. Lord, A. Thomas, N. Treat, M. Forkin, R. Bain, P. Dulac, C. H. Behroozi, T. Mamutov, J. Fongheiser, N. Kobilansky, S. Washburn, C. Truesdell, C. Lee, P. H. Schmaelzle, *Nature* **2021**, *598*, 611.
[10] T. Oki, S. Kanae, *Science* **2006**, *313*, 1068.
[11] M. Ejeian, R. Z. Wang, *Joule* **2021**, *5*, 1678.
[12] Y. Tu, R. Wang, Y. Zhang, J. Wang, *Joule* **2018**, *2*, 1452.
[13] N. Hanikel, M. S. Prévot, O. M. Yaghi, *Nat. Nanotechnol.* **2020**, *15*, 348.
[14] H. Lu, W. Shi, Y. Guo, W. Guan, C. Lei, G. Yu, *Adv. Mater.* **2022**, *34*, 2110079.
[15] Y. Song, M. Zeng, X. Wang, P. Shi, M. Fei, J. Zhu, *Adv. Mater.* **2024**, *36*, 2209134.
[16] A. Entezari, O. C. Esan, X. Yan, R. Wang, L. An, *Adv. Mater.* **2023**, *35*, 2210957.
[17] H. Shan, C. Li, Z. Chen, W. Ying, P. Poredoš, Z. Ye, Q. Pan, J. Wang, R. Wang, *Nat. Commun.* **2022**, *13*, 5406.
[18] Y. Song, N. Xu, G. Liu, H. Qi, W. Zhao, B. Zhu, L. Zhou, J. Zhu, *Nat. Nanotechnol.* **2022**, *17*, 857.
[19] H. Shan, P. Poredoš, Z. Ye, H. Qu, Y. Zhang, M. Zhou, R. Wang, S. C. Tan, *Adv. Mater.* **2023**, *35*, 2302038.
[20] H. Kim, S. Yang, S. R. Rao, S. Narayanan, E. A. Kapustin, H. Furukawa, A. S. Umans, O. M. Yaghi, E. N. Wang, *Science* **2017**, *356*, 430.
[21] N. Hanikel, X. Pei, S. Chheda, H. Lyu, W. Jeong, J. Sauer, L. Gagliardi, O. M. Yaghi, *Science* **2021**, *374*, 454.
[22] H. L. Nguyen, N. Hanikel, S. J. Lyle, C. Zhu, D. M. Proserpio, O. M. Yaghi, *J. Am. Chem. Soc.* **2020**, *142*, 2218.
[23] W. Song, Z. Zheng, A. H. Alawadhi, O. M. Yaghi, *Nat. Water* **2023**, *1*, 626.
[24] C. Sun, D. Sheng, B. Wang, X. Feng, *Angew. Chem., Int. Ed.* **2023**, *62*, e202303378.
[25] H. Qi, T. Wei, W. Zhao, B. Zhu, G. Liu, P. Wang, Z. Lin, X. Wang, X. Li, X. Zhang, J. Zhu, *Adv. Mater.* **2019**, *31*, 1903378.
[26] J. Xu, T. Li, J. Chao, S. Wu, T. Yan, W. Li, B. Cao, R. Wang, *Angew. Chem., Int. Ed.* **2020**, *59*, 5202.
[27] F. Ni, P. Xiao, N. Qiu, C. Zhang, Y. Liang, J. Gu, J. Xia, Z. Zeng, L. Wang, Q. Xue, T. Chen, *Nano Energy* **2020**, *68*, 104311.
[28] R. Li, Y. Shi, M. Wu, S. Hong, P. Wang, *Nat. Sustainable* **2020**, *3*, 636.
[29] J. Guo, Y. Zhang, A. Zavabeti, K. Chen, Y. Guo, G. Hu, X. Fan, G. K. Li, *Nat. Commun.* **2022**, *13*, 5046.
[30] X. Zhou, H. Lu, F. Zhao, G. Yu, *ACS Mater. Lett.* **2020**, *2*, 671.
[31] F. Ni, P. Xiao, C. Zhang, T. Chen, *Matter* **2022**, *5*, 2624.
[32] Y. Guo, J. Bae, Z. Fang, P. Li, F. Zhao, G. Yu, *Chem. Rev.* **2020**, *120*, 7642.
[33] C. Lei, Y. Guo, W. Guan, H. Lu, W. Shi, G. Yu, *Angew. Chem., Int. Ed.* **2022**, *61*, e202200271.
[34] G. Graeber, C. D. Díaz-Marín, L. C. Gaugler, Y. Zhong, B. El Fil, X. Liu, E. N. Wang, *Adv. Mater.* **2024**, *36*, 2211783.
[35] S. Aleid, M. Wu, R. Li, W. Wang, C. Zhang, L. Zhang, P. Wang, *ACS Mater. Lett.* **2022**, *4*, 511.
[36] F. Ni, N. Qiu, P. Xiao, C. Zhang, Y. Jian, Y. Liang, W. Xie, L. Yan, T. Chen, *Angew. Chem., Int. Ed.* **2020**, *59*, 19237.

[37] X. Liu, L. Zhang, B. El Fil, C. D. Díaz-Marín, Y. Zhong, X. Li, S. Lin, E. N. Wang, *Adv. Mater.* **2023**, *35*, 2211763.

[38] H. Lu, W. Shi, J. H. Zhang, A. C. Chen, W. Guan, C. Lei, J. R. Greer, S. V. Boriskina, G. Yu, *Adv. Mater.* **2022**, *34*, 2205344.

[39] F. Zhao, X. Zhou, Y. Liu, Y. Shi, Y. Dai, G. Yu, *Adv. Mater.* **2019**, *31*, 1806446.

[40] W. Guan, Y. Zhao, C. Lei, G. Yu, *Proc. Natl. Acad. Sci. USA* **2023**, *120*, e2308969120.

[41] H. Shan, Z. Zeng, X. Yang, P. Poredoš, J. Yu, Z. Chen, R. Wang, *ACS Energy Lett.* **2023**, *8*, 5184.

[42] C. D. Díaz-Marín, L. Zhang, Z. Lu, M. Alshrah, J. C. Grossman, E. N. Wang, *Nano Lett.* **2022**, *22*, 1100.

[43] W. Guan, C. Lei, Y. Guo, W. Shi, G. Yu, *Adv. Mater.* **2022**, *36*, 2207786.

[44] C. Zhang, P. Xiao, D. Zhang, F. Ni, J. Gu, Q. Liu, S.-W. Kuo, T. Chen, *Adv. Fiber Mater.* **2022**, *5*, 588.

[45] M. Xia, D. Cai, J. Feng, P. Zhao, J. Li, R. Lv, G. Li, L. Yan, W. Huang, Y. Li, Z. Sui, M. Li, H. Wu, Y. Shen, J. Xiao, D. Wang, Q. Chen, *Adv. Funct. Mater.* **2023**, *33*, 2214813.

[46] P. Zhu, Z. Yu, H. Sun, D. Zheng, Y. Zheng, Y. Qian, Y. Wei, J. Lee, S. Srebnik, W. Chen, G. Chen, F. Jiang, *Adv. Mater.* **2023**, *36*, 2306653.

[47] J. Xu, T. Li, T. Yan, S. Wu, M. Wu, J. Chao, X. Huo, P. Wang, R. Wang, *Energy Environ. Sci.* **2021**, *14*, 5979.

[48] T. Li, T. Yan, P. Wang, J. Xu, X. Huo, Z. Bai, W. Shi, G. Yu, R. Wang, *Nat. Water* **2023**, *1*, 971.

[49] M. Li, X. Dai, W. Gao, H. Bai, *Acc. Chem. Res.* **2022**, *3*, 1173.

[50] H. Wang, T. He, X. Hao, Y. Huang, H. Yao, F. Liu, H. Cheng, L. Qu, *Nat. Commun.* **2022**, *13*, 2524.

[51] H. Yao, P. Zhang, Y. Huang, H. Cheng, C. Li, L. Qu, *Adv. Mater.* **2019**, *32*, 1905875.

[52] Y. Guo, W. Guan, C. Lei, H. Lu, W. Shi, G. Yu, *Nat. Commun.* **2022**, *13*, 2761.

[53] R. Foudazi, R. Zowada, I. Manas-Zloczower, D. L. Feke, *Langmuir* **2023**, *39*, 2092.

[54] Y. Cui, Y. Wang, Z. Shao, A. Mao, W. Gao, H. Bai, *Adv. Mater.* **2020**, *32*, 1908249.

[55] J. Kim, G. Zhang, M. Shi, Z. Suo, *Science* **2021**, *374*, 212.

[56] M. Hauck, L. M. Saure, B. Zeller-Plumhoff, S. Kaps, J. Hammel, C. Mohr, L. Rieck, A. S. Nia, X. Feng, N. M. Pugno, R. Adelung, F. Schütt, *Adv. Mater.* **2023**, *35*, 2302816.

[57] Z. Wang, M. Heck, W. Yang, M. Wilhelm, P. A. Levkin, *Adv. Funct. Mater.* **2023**, 2300947.

[58] X. Li, K. Cui, T. Kurokawa, Y. N. Ye, T. L. Sun, C. Yu, C. Creton, J. P. Gong, *Sci. Adv.* **2021**, *7*, eabe8210.

[59] X. Yang, L. Cheng, Z. Zhang, J. Zhao, R. Bai, Z. Guo, W. Yu, X. Yan, *Nat. Commun.* **2022**, *13*, 6654.

[60] L. Ni, S. Xu, C. Sun, Y. Qin, Y. Zheng, J. Zhou, C. Yu, P. Pan, *ACS Macro Lett.* **2022**, *11*, 257.

[61] C. Zhang, Z. Wang, H. Zhu, Q. Zhang, S. Zhu, *Adv. Mater.* **2023**, *36*, 2308520.

[62] G. Nian, J. Kim, X. Bao, Z. Suo, *Adv. Mater.* **2022**, *34*, 2206577.

[63] C. Fan, R. M. Pashley, *J. Solution Chem.* **2015**, *44*, 131.

[64] F. Luo, X. Liang, W. Chen, S. Wang, X. Gao, Z. Zhang, Y. Fang, *Small* **2023**, *19*, 2304477.

[65] F. Luo, X. Liang, W. Chen, S. Wang, X. Gao, Z. Zhang, Y. Fang, *Chem. Eng. J.* **2023**, *465*, 142891.

[66] N. Hanikel, M. S. Prévot, F. Fathieh, E. A. Kapustin, H. Lyu, H. Wang, N. J. Diercks, T. G. Glover, O. M. Yaghi, *ACS Cent. Sci.* **2019**, *5*, 1699.

[67] C. Sun, Y. Zhu, P. Shao, L. Chen, X. Huang, S. Zhao, D. Ma, X. Jing, B. Wang, X. Feng, *Angew. Chem., Int. Ed.* **2023**, *62*, e202217103.

[68] Y. Wang, W. Chen, J. Fu, Y. Liu, *eScience* **2023**, *3*, 100154.

[69] S. Kim, Y. Liang, S. Kang, H. Choi, *Chem. Eng. J.* **2021**, *425*, 131601.

[70] Y. Hou, Z. Sheng, C. Fu, J. Kong, X. Zhang, *Nat. Commun.* **2022**, *13*, 1227.

[71] B. Chen, S. Jing, Q. Chen, Y. Pei, T. Deng, B. Yang, C. Wang, T. Li, *Nano Energy* **2023**, *110*, 108371.

[72] Z. Yu, S. Li, J. Su, J. Zhang, D. Zhang, Z. Zhou, Z. Qin, X. Liu, Y. Lai, S. Fu, *Matter* **2023**, *6*, 3509.

[73] A. Feng, S. Mao, C. Onggowarsito, G. Naidu, W. Li, Q. Fu, *ACS Sustainable Chem. Eng.* **2023**, *11*, 5819.

[74] Y. Chen, W. Zhou, C. Zhang, X. Feng, Y. Deng, X. Chen, H. Xie, T. Wu, J.-p. Qu, *Chem. Eng. J.* **2023**, *465*, 142849.

[75] T. Lyu, Z. Wang, R. Liu, K. Chen, H. Liu, Y. Tian, *ACS Appl. Mater. Interfaces* **2022**, *14*, 32433.

[76] T. Hatakeyama, A. Yamauchi, H. Hatakeyama, *Eur. Polym. J.* **1984**, *20*, 61.

[77] T. Ikeda-Fukazawa, N. Ikeda, M. Tabata, M. Hattori, M. Aizawa, S. Yunoki, Y. Sekine, *J. Polym. Sci., Part B: Polym. Phys.* **2013**, *51*, 1017.

[78] V. Gun'ko, I. Savina, S. Mikhalovsky, *Gels* **2017**, *3*, 37.

[79] R. Li, Y. Shi, M. Alsaedi, M. Wu, L. Shi, P. Wang, *Environ. Sci. Technol.* **2018**, *52*, 11367.

[80] J. Wang, C. Deng, G. Zhong, W. Ying, C. Li, S. Wang, Y. Liu, R. Wang, H. Zhang, *Cell Rep. Phys. Sci.* **2022**, *3*, 100954.

[81] H. Zhang, Z. Zhou, J. Du, X. Pei, L. Zhou, *J. Clean Prod.* **2023**, *416*, 137897.

[82] Z. Zhang, Y. Wang, Z. Li, H. Fu, J. Huang, Z. Xu, Y. Lai, X. Qian, S. Zhang, *ACS Appl. Mater. Interfaces* **2022**, *14*, 55295.

[83] M. Wu, R. Li, Y. Shi, M. Altunkaya, S. Aleid, C. Zhang, W. Wang, P. Wang, *Mater. Horiz.* **2021**, *8*, 1518.